

# MULTI-RESPONSE OPTIMIZATION OF THE ELECTRICAL DISCHARGE DRILLING OPERATION: A TRADE-OFF RELATION BETWEEN THE QUALITY AND EFFICIENCY

Tat Khoa-Doan<sup>1</sup>, An-Le Van<sup>2\*</sup>, Trung-Thanh Nguyen<sup>1</sup>

<sup>1</sup> Faculty of Mechanical Engineering, Le Quy Don Technical University, Hanoi, Vietnam

<sup>2</sup> Faculty of Engineering and Technology, Nguyen Tat Thanh University, Ho Chi Minh City, Vietnam

\* Ivan@ntt.edu.vn

In this work, the tool rotational speed ( $T$ ), dielectric pressure ( $W$ ), feed rate ( $F$ ), and voltage ( $V$ ) of the electrical discharge drilling (EDD) operation are optimized to decrease the extension of the drilled hole ( $EH$ ) and improve the material removal rate ( $MRR$ ). The Kriging models were utilized to present performance measures, while the Entropy approach and improved quantum-behaved particle swarm optimization algorithm (IQPSO) algorithm were employed to compute the weights and determine optimal factors. The findings presented that the optimal  $T$ ,  $W$ ,  $F$ , and  $V$  are 550 rpm, 36 kg/cm<sup>2</sup>, 30  $\mu$ m/s, and 70 V, respectively. The  $EH$  is reduced by 33.0%, while the  $MRR$  is enhanced by 39.4%, as compared to the common values. The Kriging models provided acceptable accuracy for the prediction purpose. The  $V$  and  $F$  had significant impacts on the  $EH$  and  $MRR$ . The optimal data could be utilized to enhance the performance measures for the practical EDD process. The method comprising the Kriging, Entropy, and IQPSO was a prominent solution to deal with complicated optimization issues for the EDD operation.

Keywords: EDD, extension,  $MRR$ , IQPSO, parameters

## 1 INTRODUCTION

The EDD is widely employed to produce small holes for different materials. The material is melted and evaporated using high discharging energy, while the dielectric medium is applied to flush out the debris. The small dimensions can be fabricated due to non-contacting between the workpiece and tool and zero-machining force. The low consumables, the high accuracy of the machined parts, and less investment are considerable advantages.

Different EDD operations have been considered and optimized to enhance performance measures. The traditional responses are the  $EH$ , taper ( $TP$ ), hole roughness ( $HR$ ), material removal rate ( $MRR$ ), tool wear rate ( $TR$ ), hole circularity ( $HC$ ), processing time ( $TM$ ), and machining rate ( $RD$ ). The optimal data of the spindle speed ( $T$ ), voltage ( $V$ ), and feed rate ( $F$ ) of the EDD Inconel 718 were selected using the response surface methodology (RSM) and genetic algorithm [1]. The authors stated that the  $HR$  was decreased by 36.8%, as compared to initial values. Ramaswamy and Perumal emphasized that the  $HC$  of the drilled composite was highly influenced by pulse-on time ( $O$ ), while the current ( $I$ ) has the most dominant effect on  $MRR$  and  $TR$  [2]. The impacts of the EDD factors on the  $TM$ ,  $EH$ ,  $TP$ , and  $MRR$  of the drilled Ti-6Al-7N were investigated [3]. The results indicated that the optimal  $V$ ,  $R$ , and capacitance ( $pF$ ) were 80 V, 100 pF, and 15  $\mu$ m/s, respectively. Pragadish et al. presented that the  $MRR$  of 9.69 mm<sup>3</sup>/min and a  $TR$  of 1.09 mm<sup>3</sup>/min of the drilled silicon were obtained using the cardanol oil [4]. Chiara Ravasio et al. indicated that demineralized water enhanced the  $MRR$ , while hydrocarbon oil decreased  $EH$  and  $TP$  [5]. The optimal data of the  $I$ ,  $T$ , and water pressure ( $W$ ) of the drilled AISI 304 were selected using ANN models [6]. The results indicated that the reductions in the  $HC$ ,  $TP$ , and  $TR$  were 24.6%, 18.5%, and 32.4%, respectively. The  $TR$  and  $EH$  of the drilled Inconel 718 were decreased by 24.8% and 34.7%, respectively with the optimal  $I$  and  $O$  [7]. Ahmed et al. indicated that the brass electrode enhanced by 26.2%  $MRR$  and copper tungsten decreased by 18.6%  $TR$  [8]. The  $MRR$ ,  $EH$ , and  $HR$  of the drilled stainless steel could be improved using the elliptical electrode [9]. The grey relational analysis was used to decrease the  $TP$  and  $HC$  of the drilled Nimonic-90 Alloy [10]. The results indicated that the  $I$ ,  $W$ ,  $O$ , and pulse-off time ( $FO$ ) were 10Amp, 60 bar, 8  $\mu$ s, and 7  $\mu$ s, respectively.

The  $MRR$  was improved by 12.8% and the  $TR$  was reduced by 10.6% with the aid of the water [11]. The vibration-assisted EDD process increased by 160%  $MRR$  and decreased 48.6%  $HR$  of the drilled Al-Tib2 [12]. A novel KBSI approach decreased 36.2%  $EH$  and 42.8%  $TP$  for the cooling holes [13]. The optimal  $I$ ,  $O$ ,  $FO$ , and  $W$  were selected with the support of the ANN model for improving the  $MRR$ ,  $TR$ ,  $HC$ , and  $TP$  [14]. A novel dielectric was proposed to decrease the  $TM$  for a set of drilled holes [15]. The authors stated that the productivity was increased by 26.8% for the 100 holes. The  $TR$  and  $RD$  of the drilled Nimonic 80A could be improved with the aid of the RSM approach [16]. Wang et al. emphasized that an improved genetic algorithm enhanced the EDD efficiency of film holes [17]. The  $MRR$ ,  $TR$ , and  $HC$  of the drilled Mg alloys could be enhanced using the optimal  $I$ ,  $O$ , and  $F$  [18]. The  $HC$  of the drilled Inconel 718 was affected by the  $I$  and  $O$ , respectively [19]. D'Urso et al. concluded that the  $EH$  and  $TP$  of the drilled alloy could be decreased using the carbide electrode [20]. Jacob et al. indicated that the double-helical electrode increased the  $MRR$  and reduced the  $TR$  and  $TP$  for the drilled Ti-6Al-4V [21]. However, the influences of the  $T$ ,  $W$ ,  $F$ , and  $V$  on the  $EH$  and  $MRR$  for the drilled hole of the stainless steel have not been

presented. The *EH* and *MRR* models for the EDD operation did not develop. Moreover, the optimal EDD process parameters have not been selected to boost the quality and productivity indicators.

The next section presents the optimization approach. The experimental setting and discussions are then shown. Finally, the scientific conclusions will be presented.

## 2 OPTIMIZATION APPROACH

The illustration of the the drilled hole is presented in Fig. 1.

The *EH* (mm) value is computed as:

$$EH = \frac{TD - DE}{2} \quad (1)$$

where *TD* (mm) and *DE* (mm) are the average top diameter and tool diameter, respectively.

The *MRR* (mm<sup>3</sup>/s) is computed as:

$$MRR = \frac{\Pi(TD + BD)^2 L}{16t} \quad (2)$$

where *t* (s), *BD* (mm), and *L* (mm) are the drilling time, the average bottom diameter and machined depth, respectively.

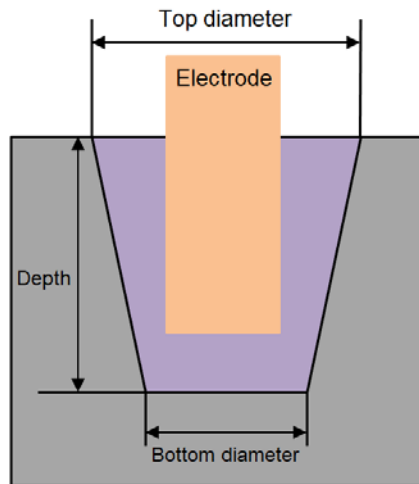


Fig. 1. The illustration of the drilled hole

In this investigation, EDD variables, including the *T*, *W*, *F*, and *V* are listed as optimization parameters (Table 1). The *T*, *F*, and *V* ranges are chosen according to the manual book of the EDD machine. The *W* ranges are determined using the features of the utilized pump. These ranges are verified with the aforementioned works and mechanical experts. The optimizing problem is presented as:

Find  $X = (T, W, F, \text{ and } V)$ ;

Minimizing *EH* and maximizing *MRR*;

Constraint:  $300 \leq T \leq 600$  rpm;  $30 \leq W \leq 90$  kg/cm<sup>2</sup>;

$30 \leq F \leq 60$  μm/s;  $30 \leq V \leq 70$  V.

Table 1. Process parameters of the EDD operation

Parameters	Levels
<i>T</i> -Tool speed (rpm)	300-450-600
<i>W</i> - Pressure of the water (kg/cm <sup>2</sup> )	30-60-90
<i>F</i> -Feed rate (μm/s)	30-45-60
<i>V</i> -Discharge voltage (V)	30-50-70

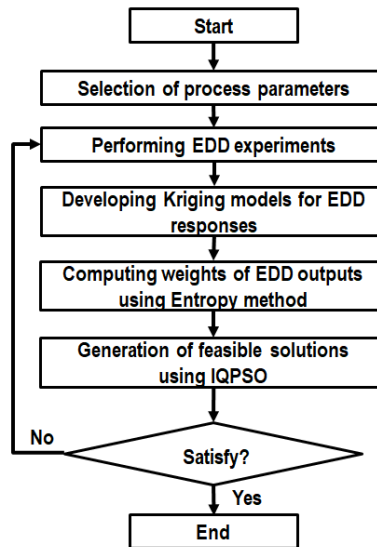


Fig. 2. Optimization approach

Step 1: Executing EDD experiments using the Box-Behnken design [22, 23].

Step 2: The Kriging models of the outputs are developed regarding EDD process parameters.

For the Kriging approach, the predictive values- $y(x)$  is expressed as:

$$y(x) = f(x)^T \beta + z(x) \tag{3}$$

where  $x$  and  $\beta$  are the input and regression coefficient, respectively.  $z(x)$  is a random data, which is presented using the following properties:

$$\begin{cases} E[z(x)] = 0 \\ Var[z(x)] = \sigma^2 \\ E[z(x^i), z(x)] = \sigma^2 R \end{cases} \tag{4}$$

where  $R$  presents the correlation matrix.

The Gaussian function is employed as the correlation function and expressed as:

$$\rho_{ij} = \exp(-\sum_{h=1}^n \theta_h |x_h^i - x_h^j|^2), i, j = 1, 2, \dots, m \tag{5}$$

where  $\theta$  and  $n$  are the unknown parameter and dimension of the sample point, respectively.

The predictive model is expressed as:

$$\hat{y}(x) = C^T(x)Y \tag{6}$$

where  $Y$  is the response vector.

The predictive deviation is expressed as:

$$\hat{y}(x) - y(x) = c^T z - z + (F^T c - f(x))^T \beta \tag{7}$$

Step 3: The weight of each response is computed using the entropy method.

The normalized objective ( $n_{ij}$ ) is calculated as:

$$n_{ij} = \frac{r_{ij}}{\sum_{i=1}^m r_{ij}} \tag{8}$$

The entropy data ( $ED_j$ ) is calculated as:

$$ED_j = -\frac{\sum_{j=1}^m n_{ij} \times \ln n_{ij}}{\ln n} \tag{9}$$

The calculated weight ( $\omega_i$ ) is expressed as:

$$\omega_i = \frac{1 - ED_j}{\sum_{j=1}^n (1 - ED_j)} \tag{10}$$

Step 4: Determination of the optimal inputs and responses using the IQPSO.

In this work, the IQPSO combining the QPSO and the Cauchy-Lorentz distribution (CL) is utilized to find the global solution. The working principle of the IQPSO is presented in Fig. 3.

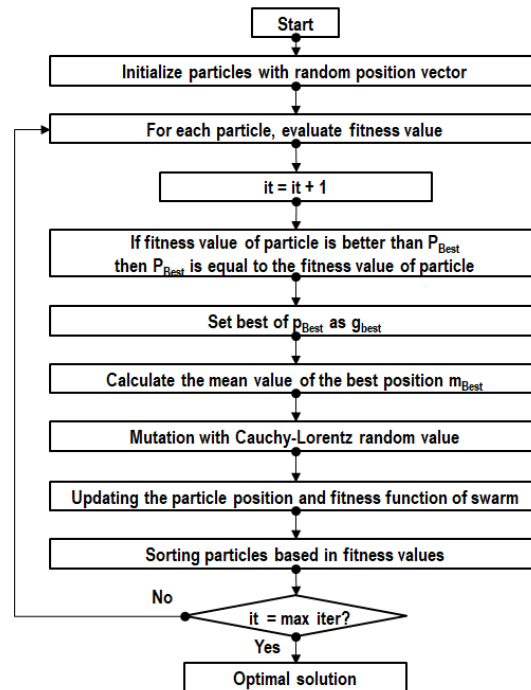


Fig. 3. Operating procedure of the IQPSO

In the QPSO, the position of each particle is expressed as:

$$x_{i,j}(t+1) = p_{i,j}(t) - \alpha(m_{besti,j}(t) - x_{i,j}(t)) \ln\left(\frac{1}{u}\right) \quad \text{If } k \geq 0.5 \quad (11)$$

$$x_{i,j}(t+1) = p_{i,j}(t) + \alpha(m_{besti,j}(t) - x_{i,j}(t)) \ln\left(\frac{1}{u}\right) \quad \text{If } k < 0.5 \quad (12)$$

$$p_{i,j}(t+1) = \lambda p_{i,j}(t) + (1 - \lambda) G_j(t) \quad (13)$$

$$m_{besti,j}(t) = \frac{1}{N} \sum_{i=1, j=1}^{N, M} P_{i,j}(t) \quad (14)$$

The probability density function ( $f(x)$ ) of the CL is expressed as:

$$f(x, x_o, \gamma) = \frac{1}{\pi} \left( \frac{\lambda}{(x - x_o)^2 + \gamma^2} \right) \quad (15)$$

where  $x_o$  and  $\gamma$  are the peak of the distribution and the scale parameter, respectively.

In the mutation stage, each vector is combined with the random value ( $D(\cdot)$ ) of the CL, which is expressed as:

$$x' = x + \lambda D(\cdot) \quad (16)$$

where  $x'$  presents the updated position.

The convergence of the IQPSO is improved using natural selection, which is expressed as:

$$F(X(t)) = \{F(x_1(t)), F(x_2(t)), \dots, F(x_N(t))\} \quad (17)$$

where  $X(t)$  and  $F(X(t))$  are the position and fitness function of each particle, respectively.

The particles are sorted based on fitness values, which is expressed as:

$$F(X'(t)) = \{F(x'_1(t)), \dots, F(x'_N(t))\} \quad (18)$$

$$X'(t) = \{x'_1(t), \dots, x'_N(t)\}$$

In the next iteration, the updated positions of the particle are expressed as:

$$X'(t) = \{x''_1(t), x''_2(t), \dots, x''_S(t)\} \quad (19)$$

$$X''_k(t) = \{x'_1(t), x'_2(t), \dots, x'_Z(t)\}$$

Table 2. Chemical compositions of the SS304

Elements	C	Si	Mn	P	S	Cr	Ni	N	Fe
%	0.051	0.57	1.75	0.028	0.005	18.18	8.48	0.05	Balance

### 3 EXPERIMENTAL FACILITIES

The brass tool having a diameter of 1.4 mm is utilized, while each specimen having a length of 16 mm, a height of 32 mm, and a width of 18 mm is employed. The stainless steel entitled SS304 having a higher carbon percentage is selected as the workpiece due to extensive applications in the pressure vessels, heat exchangers, and power generation industry. The chemical compositions of the SS304 are presented in Table 2.

The experiments are conducted in a CNC EDD machine (Fig. 4). The electrode is linearly fed downwards into the workpiece using a servo motor. The deionized water is injected using internal and side flushing to remove the debris. The CMM machine is used to measure the drilled dimensions.



Fig. 4. Experimental setting for the EDD operation

A higher diameter of the top hole is produced with an increased  $V$  (Fig. 5a), as compared to the low one (Fig. 5b). Similarly, a higher machined depth is produced with an increased  $V$  (Fig. 5c) in comparison with a low one (Fig. 5d). At a low  $V$ , a smooth surface with small cracks and small voids is found (Fig. 5e). A higher  $V$  causes higher sparking, leading to larger cracks and bigger voids (Fig. 5f).

## 4 RESULTS AND DISCUSSIONS

### 4.1 Development of the Kriging-based EH and MRR models

The experimental outcomes for the EDD operation are presented in Table 3. The coefficients of the Kriging-based EH and MRR models are presented in Table 4.

Analyzed percentages of EDD factors for the EH are presented in Table 5. Computed percentages of the  $T$ ,  $W$ ,  $F$ , and  $V$  are 3.69%, 3.51%, 11.09%, and 13.30%, respectively (Fig. 6). Computed percentages of the  $TW$ ,  $WF$ ,  $TV$ ,  $WF$ , and  $WV$  are 2.49%, 4.62%, 4.48%, 587%, and 12.19%, respectively. Computed percentages of the  $T2$ ,  $W2$ ,  $F2$ , and  $V2$  are 11.84, 13.17%, 6.51%, and 5.19%, respectively. The  $R^2$  of 0.9762 revealed that the developed EH model is adequate.

Analyzed percentages of EDD factors for the MRR are presented in Table 6. Computed percentages of the  $T$ ,  $W$ ,  $F$ , and  $V$  are 3.30%, 5.14%, 26.59%, and 31.18%, respectively (Fig. 7). Computed percentages of the  $TV$  and  $WF$  are 6.88% and 3.21%, respectively. Computed percentages of the  $T2$  and  $W2$  are 11.92% and 10.09%, respectively. The  $R^2$  of 0.9784 revealed that the developed MRR model is adequate.

Table 7 presents comparisons between the experimental and predictive values for the Kriging models. Low deviations (less than 5.0%) indicate that the proposed correlations are accurate.

### 4.2 Parametric influences

The  $EH$  has two contradictory trends, including an increment (17.3%) and a reduction (18.7%) when the  $T$  changes (Fig. 8a). A higher  $T$  increases the fluid circulation, leading to effective discharge energy; hence, a higher  $EH$  is produced. A further  $T$  decreases the drilling time, resulting in ineffective sparking; hence, the  $EH$  reduces.

The  $EH$  has two contradictory trends, including a relative increment (19.2%) and a reduction (25.2%) when the  $W$  changes (Fig. 8b). A higher  $W$  increases flow speed, leading to sustained sparking; hence,  $EH$  increases. A further  $W$  decreases the discharging time leading to ineffective discharge energy; hence, the  $EH$  reduces.

The  $EH$  has a relative increment (52.4%) when the  $F$  changes (Fig. 8c). A higher  $F$  increases the number of sparks per unit of time and more material is removed; hence, more residual particles are flushed out. This leads to higher debris distribution in more side sparking; hence, a higher  $EH$  is produced.

The *EH* has a relative increment (13.6%) when the *V* changes (Fig. 8d). A higher *V* increases the intensity of discharge energy, leading to more material removal. The sparks along the sidewalls of the drilled hole are produced due to the interactions between the electrode and residual particles, resulting in higher entry hole diameters; hence, the *EH* increases.

The *MRR* has two contradictory trends, including an increment (10.5%) and a reduction (3.5%) when the *T* changes (Fig. 9a). A higher *T* increases the fluid circulation, leading to effective sparking; hence, the *MRR* increases. A further *T* causes a faster fluid, leading to incomplete sparking; hence, the *MRR* decreases.

The *MRR* has two contradictory trends, including an increment (26.8%) and a reduction (11.2%) when the *W* changes (Fig. 9b). An increased *W* causes a higher flushing impact, leading to effective sparking; hence, the *MRR* increases. A further *W* causes excessive fluid speed, leading to a reduction in the drilling time; hence, the *MRR* decreases.

Table 3. Experimental outcomes for the EDD operation

No.	<i>T</i> (rpm)	<i>W</i> (kg/cm <sup>2</sup> )	<i>F</i> (μm/s)	<i>V</i> (V)	<i>EH</i> (μm)	<i>MRR</i> (mm <sup>3</sup> /s)
Experimental data for optimizing and developing predictive models						
1	600	90	45	50	331	0.6889
2	450	90	45	70	423	0.8865
3	300	60	45	30	313	0.6041
4	300	60	30	50	277	0.8246
5	600	30	45	50	288	0.5338
6	300	60	60	50	389	0.4098
7	450	90	60	50	351	0.7006
8	450	60	45	50	402	0.8123
9	450	60	45	50	403	0.8193
10	450	60	45	50	401	0.8178
11	450	60	30	70	361	1.1165
12	450	60	45	50	402	0.8188
13	450	60	30	30	285	0.7415
14	450	60	60	30	347	0.4905
15	600	60	45	30	279	0.4013
16	450	30	45	70	315	0.8332
17	600	60	30	50	318	0.8771
18	450	30	30	50	261	0.8441
19	450	90	30	50	321	0.7973
20	600	60	60	50	367	0.5854
21	300	30	45	50	297	0.4189
22	600	60	45	70	408	0.9667
23	450	90	45	30	257	0.5882
24	450	30	45	30	315	0.3588
25	450	30	60	50	371	0.3706
26	450	60	60	70	451	0.7767
27	300	60	45	70	381	0.6219
28	300	90	45	50	306	0.5142
29	450	60	45	50	399	0.8131
Experimental data for testing models						
30	400	40	40	40	335	0.6718
31	500	50	50	60	412	0.8248
32	350	35	40	45	321	0.6297
33	550	45	50	55	381	0.7273
34	530	65	55	60	428	0.8326

No.	$T$ (rpm)	$W$ (kg/cm <sup>2</sup> )	$F$ ( $\mu$ m/s)	$V$ (V)	$EH$ ( $\mu$ m)	$MRR$ (mm <sup>3</sup> /s)
35	380	75	52	55	408	0.7153
36	420	85	48	40	330	0.6901

Table 4. The values of Kriging model parameters

Res.	$T$	$W$	$F$	$V$	$\beta$
$EH$	0.134	0.1391	0.1445	0.0930	-0.648
$MRR$	0.086	0.1936	0.1406	0.1088	-1.105

Table 5. Computed ANOVA results for the  $EH$ 

So.	SS	MS	F value	p-value
Model	78743.45	5624.53	41.01	< 0.0001
$T$	18304.62	18304.62	133.48	< 0.0001
$W$	17411.71	17411.71	126.97	< 0.0001
$F$	55013.08	55013.08	401.18	< 0.0001
$V$	65961.13	65961.13	481.01	< 0.0001
$TW$	12351.90	12351.90	90.07	0.0042
$TF$	22917.98	22917.98	167.12	< 0.0001
$TV$	22229.94	22229.94	162.11	< 0.0001
$WF$	29118.73	29118.73	212.34	< 0.0001
$WV$	60469.74	60469.74	440.97	< 0.0001
$FV$	10169.23	10169.23	74.15	0.0038
$T^2$	58723.61	58723.61	428.23	< 0.0001
$W^2$	65341.05	65341.05	476.49	< 0.0001
$F^2$	32293.52	32293.52	235.49	< 0.0001
$V^2$	25740.56	25740.56	187.71	< 0.0001
Res.	1919.78	1919.78		
Cor.	80663.24			

R<sup>2</sup>: 0.9762; Adj. R<sup>2</sup>: 0.9624; Pred. R<sup>2</sup>: 0.9542

Table 6. Computed ANOVA results for the  $MRR$ 

So.	SS	MS	F value	p-value
Model	1.0469	0.0748	43.99	< 0.0001
$T$	0.0360	0.0360	21.18	< 0.0001
$W$	0.0560	0.0560	32.94	< 0.0001
$F$	0.2900	0.2900	170.59	< 0.0001
$V$	0.3400	0.3400	200.00	< 0.0001
$TF$	0.0038	0.0038	2.23	0.0425
$TV$	0.0750	0.0750	44.12	< 0.0001
$WF$	0.0350	0.0350	20.59	< 0.0001
$WV$	0.0078	0.0078	4.56	0.0065
$T^2$	0.1300	0.1300	76.47	< 0.0001
$W^2$	0.1100	0.1100	64.71	< 0.0001
Res.	0.0231	0.0017		
Cor.	1.0700			

R<sup>2</sup>: 0.9784; Adj. R<sup>2</sup>: 0.9632; Pred. R<sup>2</sup>: 0.9508

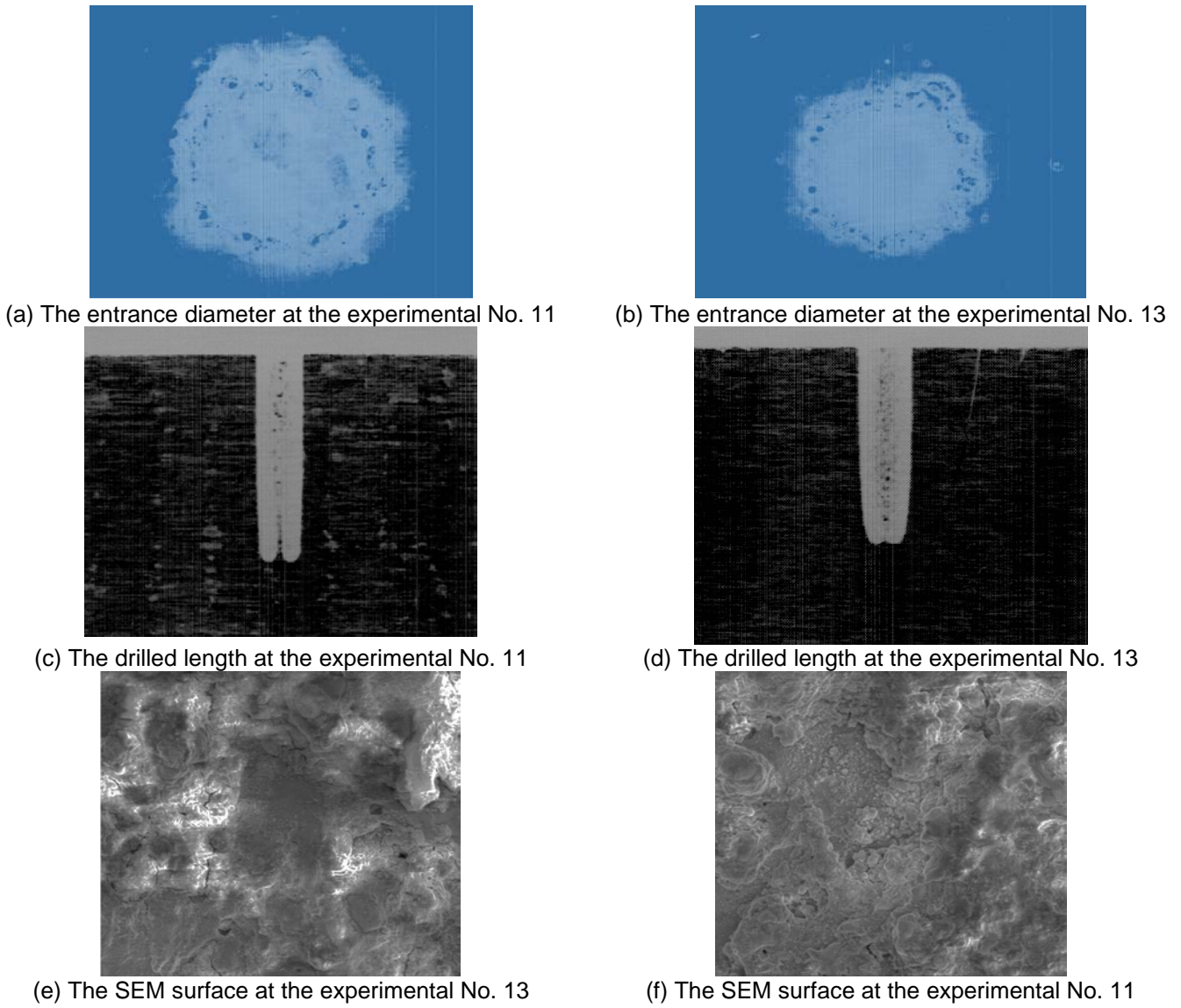


Fig. 5. Experimental outcomes at various parameters

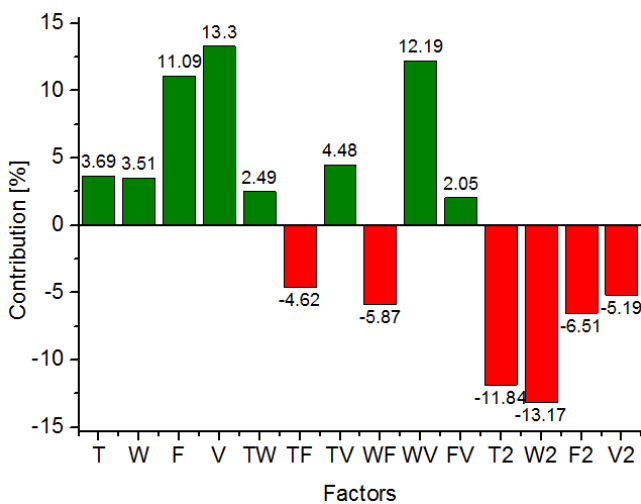


Fig. 6. Parametric contributions for the *EH* model

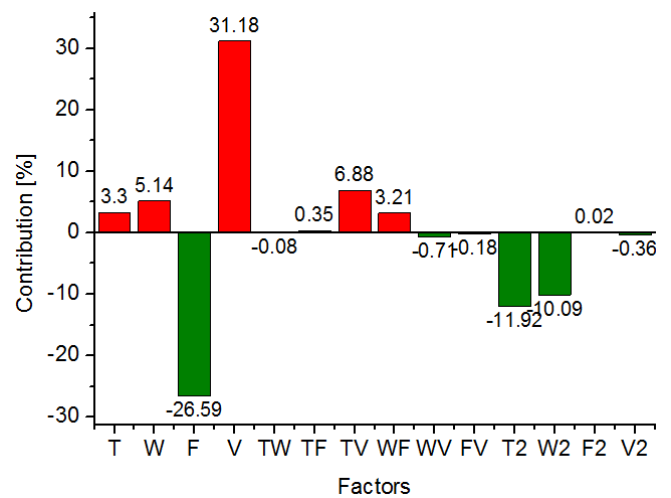


Fig. 7. Parametric contributions for the *MRR* model

Table 7. Comparisons between the experimental and predictive values

Responses		Experimental No.						
		30	31	32	33	34	35	36
Experiments	EH	335	412	321	381	428	408	330
	MRR	0.6718	0.8248	0.6297	0.7273	0.8326	0.7153	0.6901
Predictions	EH	339	408	319	378	425	411	332
	MRR	0.6732	0.8268	0.6275	0.7236	0.8364	0.7182	0.6916
Absolute errors (%)	EH	-1.19	0.97	0.62	0.79	0.70	-0.74	-0.61
	MRR	-0.21	-0.24	0.35	0.51	-0.46	-0.41	-0.22

The *MRR* causes a relative reduction (65.5%) when the *F* changes (Fig. 9c). A higher *F* decreases the processing time between the electrode and material, leading to ineffective sparking; hence, the *MRR* decreases. Practically, an increased *F* causes improper flushing impact, leading to larger exit diameters of the drilled hole; hence, the *MRR* decreases.

The *MRR* has an increment (56.3%) when the *V* changes (Fig. 9d). A higher *V* increases the intensity of the spark, leading to higher material removal. These residual particles are distributed in side walls near the entry diameter; hence, the *MRR* increases.

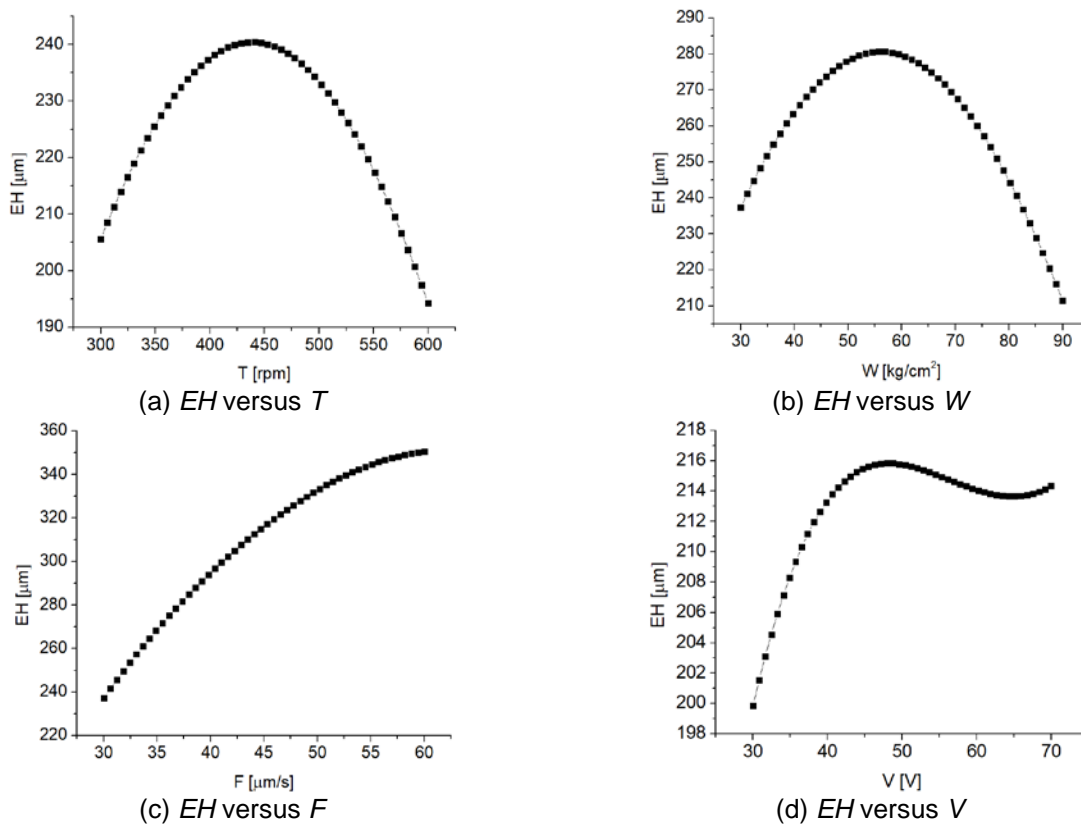
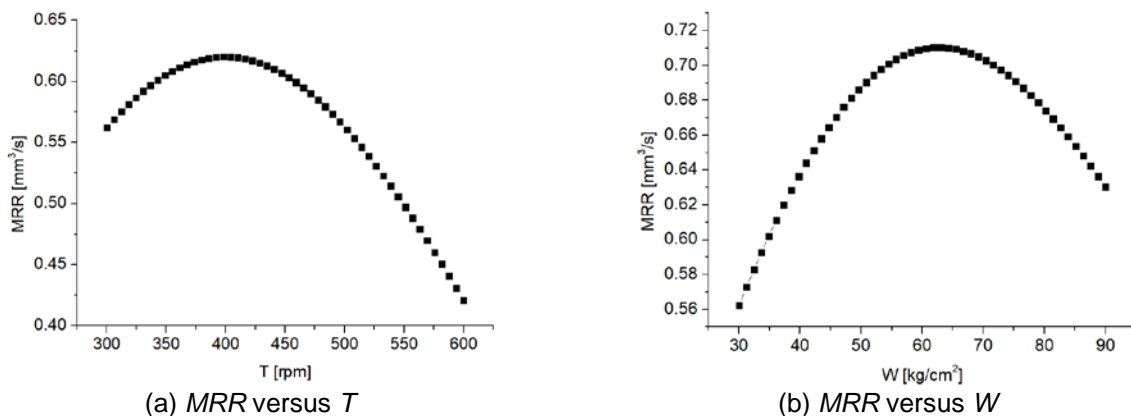
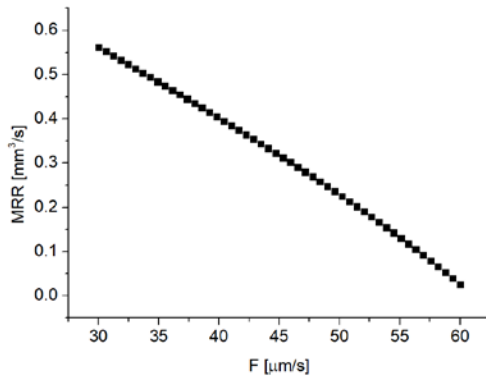
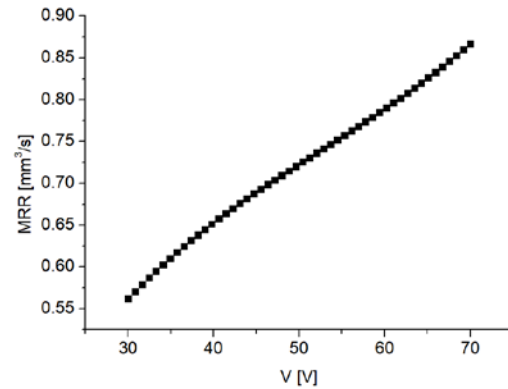


Fig. 8. The impacts of EDD parameters on the EH



(c) *MRR* versus *F*(d) *MRR* versus *V*Fig. 9. The impacts of EDD parameters on the *MRR*

### 4.3 Optimization data

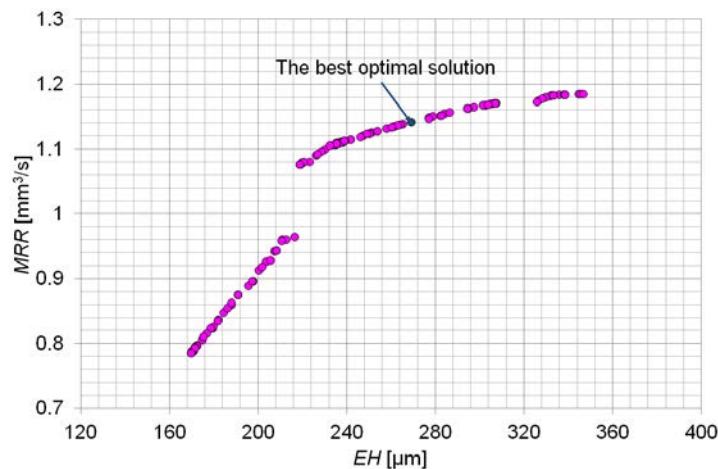


Fig. 10. The Pareto front produced by the IQPSO

As a result, the computed weight values of the *EH* and *MRR* are 0.56 and 0.44, respectively.

The Pareto graph generated by IQPSO is depicted in Fig. 10. It can be stated that a higher *MRR* leads to an increased *EH*. As a result, the optimum findings generated by the IQPSO of the *T*, *W*, *F*, and *V* are 550 rpm, 36 kg/cm<sup>2</sup>, 30 μm/s, and 70 V, respectively. The reduction in the *EH* is 33.0%, while the *MRR* is increased by 39.4%, as compared to the initial values (Table 8).

Table 8. Optimization process parameters and responses

Method	<i>T</i> (rpm)	<i>W</i> (kg/cm <sup>2</sup> )	<i>F</i> (μm/s)	<i>V</i> (V)	<i>EH</i> (μm)	<i>MRR</i> (mm <sup>3</sup> /s)
Common values	450	60	45	50	403	0.8193
Optimal values	550	36	30	70	270	1.1418
Improvements (%)					-33.0	39.4

### 4.4 Scientific and industrial contributions

The optimal data can be applied to improve the drilled quality and production rate.

The impacts of process parameters on the output objectives can be used to significantly enrich the technological knowledge of the EDD process.

The variety of output objectives can be considered as significant technical guidance for machine operators.

The Kriging models of the *EH* and *MRR* can be applied to estimate the outcome data of the output objectives.

## 5 CONCLUSIONS

In the current work, optimal EDD process parameters (*T*, *W*, *F*, and *V*) were selected to boost hole quality (*EH*) and production rate (*MRR*). The Kriging approach was utilized to propose EDD responses, while the IQPSO was used to produce feasible solutions. The Entropy method was utilized to find the weights of all objectives. The obtained conclusions are expressed as:

1. The low values of the *T*, *W*, *F*, and *V* were recommended to decrease the *EH*, while the highest *F* could be used. The highest data of the *T* and *F* were used to reduce the *MRR*, while the lowest *W* and *V* were mentioned.

2. For the values considered of EDD inputs, the *EH* and *MRR* increase from 257 to 451  $\mu\text{m}$  and 0.3588 to 1.1165  $\text{mm}^3/\text{s}$ , respectively.
3. With the *EH* and *MRR*, the *V* and *F* had the highest contributions.
4. The optimizing data of the *T*, *W*, *F*, and *V* are 550 rpm, 30  $\text{kg}/\text{cm}^2$ , 30  $\mu\text{m}/\text{s}$ , and 70 V, respectively. The improvements in the *EH* and *MRR* were 33.0% and 39.4%, respectively.
5. Improving hole quality and material removal rate is a significant contribution to the EDD process.
6. The energy efficiency and noise emission will be explored in future works.

## REFERENCES

- [1] Dilip, D.G. et al. (2020). Characterization and Parametric Optimization of Micro-hole Surfaces in Micro-EDD Drilling on Inconel 718 Superalloy Using Genetic Algorithm. *Arabian Journal for Science and Engineering*, vol. 45, 5057–5074. DOI: 10.1007/s13369-019-04325-4
- [2] Ramaswamy, A., Perumal, A.V. (2020). Multi-objective optimization of drilling EDD process parameters of LM13 Al alloy–10ZrB<sub>2</sub>–5TiC hybrid composite using RSM. *Journal of the Brazilian Society of Mechanical Sciences and Engineering*, vol. 42, 432. DOI: 10.1007/s40430-020-02518-9
- [3] Singh, A.K. et al. (2020). Experimental study on drilling micro-hole through micro-EDD and optimization of multiple performance characteristics. *Journal of the Brazilian Society of Mechanical Sciences and Engineering*, vol. 42, 506. DOI: 10.1007/s40430-020-02595-w
- [4] Pragadish, N. et al. (2022). Optimization of cardanol oil dielectric-activated EDD process parameters in machining of silicon steel. *Biomass Conv. Bioref.* (2022). DOI: 10.1007/s13399-021-02268-1
- [5] Ravasio, C. et al. (2023). Development of CO<sub>2</sub> efficiency index for evaluating sustainability of microelectrical discharge drilling process. *Journal of Engineering Manufacture*, vol. 237, 758-769. DOI: 10.1177/09544054221111903
- [6] Kumar, K. et al. (2019). EDD  $\mu$ -drilling in Ti-6Al-7Nb: experimental investigation and optimization using NSGA-II. *International Journal of Advanced Manufacturing Technology*, vol. 104, 2727–2738 DOI: 10.1007/s00170-019-04012-6
- [7] Machno, M. (2020). Investigation of the Machinability of the Inconel 718 Superalloy during the Electrical Discharge Drilling Process. *Materials*, vol. 13, 3392. DOI: 10.3390/ma13153392
- [8] Ahmed, A. et al. (2020). Ultrafast drilling of Inconel 718 using hybrid EDD with different electrode materials. *International Journal of Advanced Manufacturing Technology*, vol. 106, 2281–2294. DOI: 10.1007/s00170-019-04769-w
- [9] Bozdana, A., Al-Kharkhi, N. (2018). Comparative Experimental and Numerical Investigation on Electrical Discharge Drilling of AISI 304 Using Circular and Elliptical Electrodes. *Strojniški vestnik – Journal of Mechanical Engineering*, vol. 64, 269-279. DOI: 10.5545/sv-jme.2017.4806
- [10] Pandey, A.K., Gautam, G.D. (2018). Grey relational analysis-based genetic algorithm optimization of electrical discharge drilling of Nimonic-90 superalloy. *Journal of the Brazilian Society of Mechanical Sciences and Engineering*, vol. 40, 117. DOI: 10.1007/s40430-018-1045-4
- [11] Suresh, K. et al. (2022). Effect of Silane Treated Wheat Husk Biosilica (WHB) Deionized Water Dielectric on EDD Drilling of Ti-6Al-4 V Alloy. *Silicon*, vol. 14, 9143–9151. DOI: 10.1007/s12633-021-01526-1
- [12] Pandey, G.K., Yadav, S.K.S. (2022). Experimental investigation of vibration assisted electrical discharge drilling of Al-TiB<sub>2</sub>. *International Journal on Interactive Design and Manufacturing*. DOI: 10.1007/s12008-022-01002-z
- [13] Wang, J. et al. (2023). Stage identification and process optimization for fast drilling EDD of film cooling holes using KBSI method. *Advances in Manufacturing*. DOI: 10.1007/s40436-022-00434-w
- [14] Pattanayak, S. et al. (2022). CFRP composite drilling through electrical discharge machining using aluminum as fixture plate. *Journal of Mechanical Engineering Science*, vol. 236, 5468-5483. DOI:10.1177/09544062211058675
- [15] Tanjilul, M. et al. (2021). Super dielectric based edd process for drilling of inconel 718. *Materials and Manufacturing Processes*, vol. 36, 341-350. DOI: 10.1080/10426914.2020.1832682
- [16] Piyush, P., Pushpendra S.B. (2023). Experimental Investigation on Micro-Electrical Discharge Machining process for heat treated Nickel-based Nimonic 80A. *Materials and Manufacturing Processes*, 2023, vol. 38, 1-12. DOI: 10.1080/10426914.2022.2105889
- [17] Wang, J. et al. (2021). Path optimization for multi-axis EDD drilling of combustor liner cooling holes using SCGA algorithm. *Computers & Industrial Engineering*, vol. 157, 107319. DOI: 10.1016/j.cie.2021.107319
- [18] Parsana, S. et al. (2018). Machining parameter optimization for EDD machining of Mg–RE–Zn–Zr alloy using multi-objective Passing Vehicle Search algorithm. *Archives of Civil and Mechanical Engineering*, vol. 18, 799–817. DOI:10.1016/j.acme.2017.12.007

- [19] Mohanty, Chinmaya P. et al. (2016). A particle swarm approach for multi-objective optimization of electrical discharge machining process. *Journal of Intelligent Manufacturing*, vol. 27, 1171–1190. DOI:10.1007/s10845-014-0942-3
- [20] D'Urso, G. et al. (2015). Investigation on power discharge in micro-EDD stainless steel drilling using different electrodes. *Journal of Mechanical Science and Technology*, vol. 29, 4341–4349. DOI: 10.1007/s12206-015-0932-1
- [21] Jacob, K.S., Samuel, G.L. (2021). Effect of micro double helical grooved tools on performance of electric discharge drilling of Ti-6Al-4V. *Journal of Engineering Manufacture*, vol. 235, 1832-1847. DOI:10.1177/0954405421995605
- [22] Duy, Đ.V., Quang, V.D. (2022). A mathematical model for thinning rate prediction of sheet double hydro-forming. *Journal of Applied Engineering Science*, Vol. 20, 987-999. DOI: 10.5937/jaes0-35082
- [23] Nabila, D. et al. (2023). Experimental based determination and analysis of mechanical properties of aa 3003 alloy welded with friction stir lap welding process. *Journal of Applied Engineering Science*, Vol. 21, 451-461. DOI: 10.5937/jaes0-40245

*Paper submitted: 24.09.2023.*

*Paper accepted: 29.11.2023.*

*This is an open access article distributed under the CC BY 4.0 terms and conditions*